Performance Evaluation of the PC-2048: A New 15-Slice Encoded-Crystal PET Scanner for Neurological Studies

A. C. Evans, C. J. Thompson, S. Marrett, E. Meyer, and M. Mazza

Abstract—**We report initial experience with the Scanditronix PC 2048-15B, a 15-slice PET system using multicrystal/multi-PMT modules to obtain high spatial resolution. Design parameters include: crystal dimensions = 6 × 12 × 30 mm; crytal : PMT encoding = 16 : 4; ring diameter = 50.5 cm; collimator length = 9 cm; slice separation = 6.5 mm; coincidence resolving time = 20 ns. Using an orbiting ^{68}Ge rod source for transmission scans, random and scattered events are reduced by only accepting coincidence lines which intersect the instantaneous position of the source. Scatter correction of the emission data is removed with a deconvolution kernel, random and dead-time correction by use of observed singles rates. System efficiency for the direct and cross slices are 9.7 and 13.7 Kcps/(μCi/cc) from a 19 cm flood phantom. The peak count rates are 11.7/20.0 Kcps for the direct/cross slices at concentrations of 4.5/5.1 μCi/cc, respectively. Taking scatter and randoms into account, the peak noise-effective count rates are 7.1/11.3 Kcps for direct/cross slices at 3.3/3.6 μCi/cc, respectively. Random coincidences are 8–9% of the total rate at 0.8 μCi/cc. Over the radial range 0–9 cm from the ring center, radial transverse resolution (FWHM is wobble mode) is 4.6–6.4 mm and tangential transverse resolution is 4.6–5.1 mm using a Hanning filter. Over the same range, axial resolution varies from 6.1–6.2 mm in direct slices and from 5.4–7.1 mm in cross slices. This near-isotropic resolution allows collection of image volume data with no preferred direction for signal averaging errors.**

I. Introduction

We present an evaluation of the first Scanditronix PC-2048 brain PET scanner to be installed. Preliminary results were presented at the Society of Nuclear Medicine Symposium in 1989 [1]. This system, now operating routinely at the Montreal Neurological Institute, acquires 15 simultaneous slice images, covering almost the entire human brain, without couch repositioning. A fundamental design feature is the multicrystal detector module, in which 16 small crystals are mounted on two dual photomultipliers, yielding a resolution of 5–6 mm in three dimensions. An orbiting transmission source provides high quality attenuation images, which are useful for localization, as well as attenuation correction. Typical blood flow, glucose utilization, and attenuation scans on control subjects are presented.

II. System Design

The PC-2048 scanner described is installed at the Montreal Neurological Institute (MNI), where it has been in routine use since mid-1989 scanning patients and control subjects.

Manuscript received February 12, 1990; revised August 27, 1990.

The authors are with Positron Imaging Laboratories, McConnell Brain Imaging Unit, Montreal Neurological Institute, McGill University, Montreal H3A 2B4, Quebec, Canada.

IEEE Log Number 9041386.

TABLE I
Hardware Aspects of the PC-2048 Brain PET System

Ring diameter	50.5 cm
Patient aperture	27 cm
Number of direct/cross slices	8/7
Scintillation crystal type	Bismuth Germanate (BGO)
Septal thickness	3 mm
Crystal dimensions	6 × 12 × 30 mm
Crystal packing fraction	92%
Crystal separation	0.2 mm
Ring separation	1 mm
Number of crystals per ring	256
Transmission method	Orbiting ^{68}Ge rod source
Minimum wobble time	1 s
Tilt angle	±20°

A. Tomograph Configuration

The major hardware aspects of the PC-2048 are listed in Table I. The scanner is a scaled-down version of the PC-4096 body system, the performance of which was measured by Holte *et al.* [2], suitable for more efficient brain imaging. The number of detectors is reduced to half, halving the ring diameter and doubling the true count efficiency while reducing the cost and complexity. Gamma rays from beyond the adjacent slice are blocked by 3 mm thick lead (5% antimony) flat septa. The inner diameter of the septa is 30 cm. Beyond the axial field of view, led from 3 to 5 cm thick attenuates almost all external radiation.

The computer configuration for our system is based on a MicroVAX II host running VMS and a Ramtek 9465 640 × 512 pixel display processor. Newer systems use a faster MicroVAX III processor in a workstation configuration. Data is acquired on an Intel 80286 based data acquisition processor (DAP) running iRMX/286. A 32-b mini-map array processor is used for the computationally intensive parts of the reconstruction process. List mode acquisition and gantry slew (rotation about the vertical axis), which are available as options, are absent from our configuration. All host programming is in VAX Fortran 77. The DAP and MicroVAX are connected via Ethernet, and this also serves to link the host to six other systems at MNI. All power is conditioned and maintained continuously with a AT&T 10 kVA uninterruptable power supply (UPS). The host computer has three fixed disks with a combined capacity of 1.5 Gbytes, a 650 Mbyte erasable optical disk and triple-density industry standard magnetic tape for image archiving.

B. Crystal Encoding

The detector modules contain 16 bismuth germinate (BGO) crystals 30 × 12 × 6 mm in a 4 × 4 matrix optically coupled

0278-0062/91/0300-0090$01.00 © 1991 IEEE

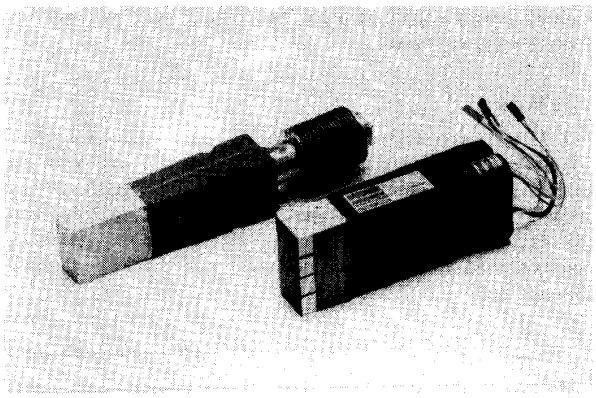

Fig. 1. The 4 × 4 crystal block with its two dual 1548 PMT's compared to a single crystal/PMT detector module from the older Therascan system at the MNI.

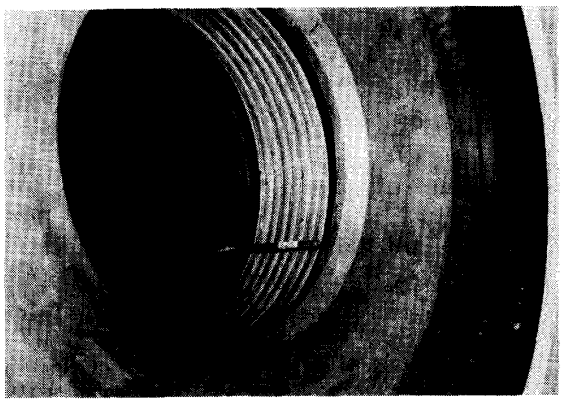

Fig. 2. The orbiting rod source in its mounted position just inside the collimators.

to two Hamamatsu R1548 dual photomultipliers (PMT's). Fig. 1 illustrates the size of the block detector relative to a single BGO detector module from one of our previous scanners [3]. Four block detectors modules, separated by a tapered lead wedge, are packed in one light-proof, easily replaceable, cassette. This contains a high voltage distribution network, dynode biasing resistors, and a buffer amplifier for each anode. The detectors are arranged on a 50.5 cm diameter ring, with 16 cassettes per ring for a total of 256 crystals around the circumference. Two banks of cassettes provide eight rings of crystals. Coincidences are detected between crystals in the same and the adjacent rings, yielding 15 scanning planes.

C. Data Sampling

The detectors, preamplifiers, and septa perform an orbital motion during "wobbled" scans to increase the density of sampling in each projection. The diameter of the wobble circle is fixed at 6 mm while the wobble speed is variable from 1 to 60 rpm. During wobbled mode, scans data from crystal pair are first projected onto a line normal to the line joining the crystal pairs and then sampled into five bins 1.2 mm wide. There are 256 (one per crystal) projections sampled at 1.2 mm. In stationary mode, the sampling would be only every 6.2 mm at the center of each projection. To improve linear sampling, odd and even projections are interleaved to yield 128 projections sampled every 3.1 mm.

D. Orbiting Transmission Source

To provide a transmission attenuation correction with considerably reduced random [4], [5] and scattered [6]–[9] events, the scanner is equipped with an orbiting rod transmission source. The source contains about 5 mCi of ^{68}Ge embedded in a gel within a 5 mm ID aluminium rod. The source orbits at 20 rpm, in a space between the tunnel defining the patient port and the septa, but does not share the wobble motion of the detectors. Fig. 2 shows the scanner with the front cover removed to expose the rod source. Transmission and emission scans can both be performed in wobbled or stationary modes. Reconstruction of wobbled emission data with stationary transmission data or vice versa is permissible, the necessary interpolation of projection data being performed automatically.

E. Gantry and Couch Features

Although the inner diameter of the collimators is 30 cm, the patient port is limited to 27 cm in diameter to allow room for the transmission source and septa wobbling. The gantry can tilt ±20°. (The length of the scanning tunnel reduces the vertical diameter with 20° tilt to 24 cm.) The couch can be moved axially either manually to position the patient, or under computer control between scans if required. The couch can be removed vertically manually when well clear of the gantry. In addition, the whole couch top can be lowered onto a large wheeled trolley, so that it can become a stretcher for patient transport or pre-scan setup in an adjacent room.

F. Blood Sampler

An automatic blood sampler employing two sets of coincident BGO crystals and a peristaltic pump [10] is provided for continuous arterial blood monitoring. This device is particularly suitable for the short duration bolus $H_2^{15}O$ blood flow studies, which otherwise require many manually collected, counted, and timed samples. The control of the blood sampling schedule is integrated into the data acquisition program, which provides a log of sample counts and times with respect to the start of scan. The blood sampler is connected to the host computer via a terminal port.

G. Data Acquisition Electronics

Salient features of the data acquisition electronics are listed in Table II. Buffered pulses from each of 512 PMT anodes are fed by coaxial cables to the discriminator rack in an adjacent room. Each discriminator board processes signals from four detector modules. Each signal is split in two. A clipped version is summed with others from the same module to activate a leading edge discriminator, which triggers a retriggerable monostable. Its duration is set by the computer for best coincidence timing. The other signal is amplified by a voltage-controlled amplifier and integrated slightly and is summed with the three others in its module for energy determination, and compared with the other signal in the same row and column in separate comparators to identify the crystal in which the incident gamma ray was absorbed. When the monostable times out, a set of comparators identify the crystal and a second set of comparators at the output of the summing amplifier validate the energy.

TABLE II
ELECTRONICS

Coincidence window	20 ns
Photomultipliers	Hamamatsu 1548 dual PMT
Crystal : PMT encoding	16 : 4
Timing	Leading edge
Energy window	300–650 keV
Energy/timing alignment	Automatic
No. coincidence circuits	One per ring-pair
Event derandomizing	64-b FIFO

There are no manual adjustments on the discriminator boards. The timing (1), gain (4), and energy selection (2) parameters are set by the data acquisition processor to preset values determined by a system optimization program. To reduce the number of digital to analog converters (DAC), the seven control voltages are output sequentially into a multiplexer which stores the control voltage for each function on a capacitor.

The timing and crystal identification signals are processed by a coincidence circuit with a selectable resolving time. When a valid coincidence occurs, the crystal pair information is saved in a first in-first out (FIFO) memory. Data words from the FIFO are sorted into parallel projections using instructions coded in a programmable read only memory (PROM). This also selects the axial and radial acceptance criteria. These acceptance criteria are fixed in our system to allow only coincidences from direct and adjacent planes, and a field of view of 30 cm. Projection data are not corrected for the gradually decreasing coincidence-chord separation with increasing radius.

In wobbled studies, the wobble information is added as a displacement along the projection. In transmission scans, the angle of the transmission source is subtracted from the projection and each event is validated by requiring near collinearity of the source and detecting crystal pair [7]. Noncollinear events are rejected to reduce scattered and random events in transmission scans. The PROM, which selects valid transmission events, accepts only 5% of the possible chords through the field of view. The wobble-phase information is not used in the selection of collinear events.

H. Software

Images are reconstructed using a standard filtered backprojection algorithm on to a 128 × 128 or 256 × 256 matrix of selectable pixel size. Data are corrected for dead-time using an empirically derived model based on the singles-rate per crystal block. Random correction is performed using the observed block singles rate and the coincidence window to calculate the random rate ($S_1 S_2 \times 2\tau$ method). Attenuation correction is done by contour finding in projection space or by using a matched transmission scan. Scattered events are removed using the deconvolution method of Bergstrom [11].

III. MATERIALS AND METHODS

Most of the experiments to evaluate the system performance were performed with a 19 cm ID, 15 cm long lucite cylinder, supplied by Scanditronix, which attaches to the couch in place of the head holder. Various inserts can be used and attached to the front plate. These include water-tight 5 cm ID cylinders, 0.5 mm stainless steel needles, and thin lucite supports for 1 mm thick hollow disks in the scanning plane. The support plate holds the cylinder horizontal, and it can be moved vertically with the couch manual controls, and axially either manually or under computer control.

A. Efficiency

To determine system efficiency, the 19 cm phantom was filled with fluorodeoxyglucose (FDG), which does not react with the lucite walls, at an initial concentration of 161 nanoCi/cc and scanned for 320 min for a mean activity of 69.4 nanoCi/cc over the scan. Random correction was performed and the remaining counts plotted used to determine the count rate per unit activity for each slice.

B. Random Fraction, Live-Time, and Count Rate Capability

To assess the behavior of the PC-2048 at high count rates, the 19 cm phantom was filled with an initial concentration of 8.5 μCi/cc of ^{11}C and scanned repeatedly in increasing frame-times of 2, 4, 6, and 8 min over 213 min or approximately 10 half-lives. The total observed count rate for each frame was then plotted against mid-time for that frame. The lowest activity frames were considered to be free from significant random or dead-time effects and were due to trues and scattered ($T + S$) events only. These data were fitted by linear regression and subtracted from the total to estimate the random component at each point. The random component R at low activities was then fitted with a quadratic function, since randoms are proportional to the square of the activity concentration. Live-time was then estimated as the ratio of observed to expected ($T + S$). Count rate capability was then determined from the saturation T rate, i.e., after removal of scattered events. The effects of noise from scattered and randoms events were accounted for by plotting the noise-effective trues rate T_{NE} versus concentration where $T_{NE} = T^2/(T + S + R)$. This empirical approach was taken to avoid any biases inherent in assumed models of dead-time behavior.

C. Axial Resolution

Three 1 mm thick hollow disks were filled with undiluted ^{68}Ga-EDTA, each disk containing approximately 1.3 μCi/cc of ^{68}Ga at the start of the scan. The disks were inserted in holes at 0, 5, and 9 cm from the center of the cylinder for the first scan and 0, 9, and 12.5 cm from the center in a second scan. The last disk holder was attached to the outside of the cylinder, clearing the scanning tunnel by 2 mm. All measurements were performed in air. The cylinder was centered in the scan field and advanced into the scanner so that the active disks were initially in scanning plane 12. One hundred 1-min data frames were collected, with the detector array stationary and a bed movement of 1 mm between frames.

Images were reconstructed on a 128 × 128 matrix using 2 mm pixels for the first study, and 3 mm pixels for the second study in order to visualize the outermost active disk. Raw data were corrected for random events and decay correction and a 5 mm Hann reconstruction filter was used. For each slice, approximately 30 sequential images contained counts as the source moved through the imaging planes. For those images, circular ROI's were placed over the three active disks and image activity as a function of axial source position obtained from each ROI in each slice. These data were analyzed to determine the slice profile at five distances from the center. The full width at half and one-tenth maximum (FWHM and FWTM) were determined by interpolation, (since in the outer regions, especially of the cross slices are not Gaussian) for each slice. In addition, the

centroid of the slice profile measured between the FWTM points was recorded to measure the interslice separation.

D. Transverse Resolution

The in-plane spatial resolution was determined using the stainless needles filled with ^{68}Ga-EDTA undiluted from a generator. The measurement was performed in air, since the purpose was to measure the intrinsic resolution rather than the normal scanning resolution, which would have included the effects of positron range from the isotope used for that study. Each needle contained about 10 μCi of ^{68}Ga. Four scans of 10 min duration were performed. The first two were performed with the needles at 0, 5, and 7.5 cm from the center, in both wobbled and stationary modes. For the second set, the needles were at 0, 9, and 12.5 cm from the center, in wobbled and stationary modes.

Each scan was reconstructed on a 256 × 256 matrix, using 1 mm pixels for the first set and 1.2 mm pixels for the latter set, in order to visualize the outer needle. Since the scans were done in air, no attenuation correction was performed. The reconstruction program provides five different reconstruction filters: Hann, Ramp, Shepp and Logan, Parz, and Hamming. Each filter and a range of cutoff frequencies, ranging from the minimum (the pixel size for wobbled studies, and 3.2 mm for stationary studies) up to 10 mm, were used to reconstruct each study.

Radial and tangential lines were drawn through the peak of each needle peak in the highest resolution image and profiles computed along these lines. The FWHM and FWTM were calculated by interpolation from the profile obtained in each slice separately and the mean and standard deviation over the five slices in which that needle was best visualized were calculated. The FWHM and the FWTM of the radial and tangential components of the intrinsic resolution (using the sharpest filter) for stationary and wobbled studies were plotted separately. The best obtainable FWHM and FWTM were measured for all filter types in the center of the field were also determined from similar measurements on at least five slices. The FWHM and FWTM of the reconstructed resolution, as a function of filter width in mm, were also plotted for the Hann filter for the central point in stationary and wobbled scanning modes.

E. Image Noise as a Function of Scan Mode and Filter Width

Patient studies are rarely reconstructed to obtain the intrinsic system resolution, a filter being applied to smooth the image for improved visualization of structures of interest. This is most often the case when analyzing the low-count images obtained in dynamic scans or bolus $H_2^{15}O$ blood flow studies. This experiment investigated the noise reduction performance of the filters provided with the PC-2048 in low-count situations, as well as assessing the noise-related merits of using stationary or wobbled scan modes. Palmer *et al.* [12] showed the images obtained from a wobbled scanner were noisier than ones which did not have to wobble to obtain the same image resolution. This is due to the fact that bins at the edge of the wobble pattern contain more counts than those in the center of the wobble pattern, and the final image noise is due to the bins with the minimum counts. On the other hand, since the wobbled mode provides improved intrinsic resolution, reconstructing wobbled images with a filter which gives the same reconstructed resolution as a stationary study should provide less noisy images. Since the wobbled images are intrinsically sharper, they must be blurred more by the reconstruction filter to yield the same resolution as the stationary mode scans [12], [13].

A 17 cm diameter cylinder containing ^{68}Ge solution with a specific activity of 50 nCi/cc was placed in the center of the scan field on a foam pad. Scans of 4 and 16 min duration in the wobbled and stationary modes were performed. These were reconstructed on a 128 × 128 matrix, using a calculated circular attenuation outline, in order to eliminate potential noise from using a transmission scan. The low activity concentration minimizes the noise due to random counts. Hence, the noise in the images is due predominantly to counting statistics, noise introduced by removal of scattered events, and the reconstruction process.

This phantom provided 400K and 600K counts in 16 min in the direct and cross slices, respectively. This is close to the number of counts obtained from typical bolus $H_2^{15}O$ blood flow studies. Thus, the noise in these images is similar to those found in real imaging situations. Images were reconstructed at a series of filter widths after correction for randoms, scatter, attenuation, and variations in detector efficiency. A circular region of interest covering the central 80% of a typical cross slice was then analyzed for standard deviation as a function of image resolution.

F. Scatter Fraction

To assess the scatter correction of the PC-2048, we performed a cool/cold spot experiment under low activity conditions so as to remove confounding effects from random events. A stock solution of ^{68}Ga was used, to both fill the 19 cm phantom and provide a separate sample which was diluted to one quarter of its initial concentration. Two inserts were then added to the phantom, one filled with the diluted solution and one containing water, to provide 25% and 0% contrast. The cool (25%) spot was centered, while the cold spot was located midway between the center and the edge of the phantom. The phantom thus provided an asymmetric activity distribution. The assembly was then scanned for 60 min and images reconstructed. Regions-of-interest 3.5 cm in diameter were located in each spot and at 7 places over the background region. Average background and cool and cold spot values were then obtained for all slices.

G. Variable Contrast Recovery

To test the overall behavior of the system under changing conditions of contrast, random fraction, and live-time, we performed a dual isotope experiment [14]. The 19 cm phantom was filled with ^{11}C while a 5 cm diameter cylindrical insert, located halfway to the edge of the phantom, was filled with ^{68}Ga and the whole assembly scanned repeatedly over 210 min, i.e., more than 10 ^{11}C half-lives. Initial concentrations were set at 6 and 0.30 μCi/cc, respectively, in the outer ^{11}C and inner ^{68}Ga compartments. The inner compartment was therefore a 5% cool spot at the beginning, with the ^{11}C: ^{68}Ga contrast ratio changing from 20:1 to 1:5 over the course of the experiment. The concentration was such that the system live-time was initially only 12%. Images were reconstructed with no decay-correction and plotted versus time in semi-log form. The low activity points were then fitted with the known half-life of the two isotopes (20.3 and 68.3 min) and the fit extrapolated to high count rates.

IV. Results

The major results obtained from the experimental program are discussed below and summarized in Table III.

TABLE III
SUMMARY OF PERFORMANCE CHARACTERISTICS

Efficiency (Direct (D) : Cross (C))	9.7 : 13.7 kcps/(μCi/cc)
Image resolution (0–9 cm)	
Transverse radial	4.6–6.4 mm FWHM
Transverse tangential	4.6–5.1 mm FWHM
Axial (D : C)	6.1–6.2 mm : 5.4–7.1 FWHM
Random fraction	10% @ 1.0 μCi/cc (19 cm flood)
Live-time	80% @ 1.0 μCi/cc (19 cm flood)
Saturation true rate (D : C)	11.7 : 20.0 kcps
Effective saturation true rate (D : C)	7.1 : 11.2 kcps
Scatter fraction	19% (19 cm diameter flood)
Typical FDG scan 45 min after 5 mCi injection:	
Counts in 15 min (D : C)	1.0 : 1.5 Million
Live-time	98%
Random fraction	2%
Typical bolus $H_2^{15}O$ blood flow study after 40 mCi injection:	
Counts in 1st min (D : C)	0.3 : 0.4 Million
Live-time	82%
Random fraction	8–9%

A. Efficiency

Fig. 3 plots the efficiency of the PC-2048 for all 15 slices. Slice 4, the central cross slice in the lower block, showed a somewhat low result but all slices exhibited the expected alternating pattern of direct/cross slice efficiency. Average values were 9.7 and 13.7 kcps/(μCi/cc) from a 19 cm diameter flood.

B. Random Fraction, Live-Time, and Count-Rate Capability

Figs. 4–7 illustrate the high count-rate behavior of the PC-2048. In Fig. 4, the apparent and dead-time corrected curves for both ($T + S$) and R components for slice 1 are plotted against activity concentration, ρ, in log–log space. The slope of the two fitted curves are fixed at 1 and 2, reflecting their respective linear and quadratic dependence on ρ. This form emphasizes the fitting at the low activity end. This analysis allows for the identification of live-time, random fraction, and noise-effective count-rate. Figs. 5 and 6 show the live-time and random fraction for components, indicating that at a ρ of 0.8 μCi/cc in a 19 cm diameter phantom, approximating the conditions of a bolus $H_2^{15}O$ blood flow study, the live-time is 82% and the random fraction is 8–9%. Fig. 7(a), (b) plot both trues and noise-effective trues versus ρ for both direct and cross slices and indicate a saturation ρ of greater than 3 μCi/cc.

C. Axial Resolution

The axial resolution for both typical true and cross slices is shown in Fig. 8 as a function of radial image position. The FWHM of the direct slices is almost constant at 6.2 mm out to 9 cm from the center of the image, while the FWHM of the cross slice varies only from 5.2 mm at the center to 6 mm at 9 cm. Only beyond 9 cm does the FWHM rise abruptly but this is outside the normal scanning region, allowing one to conclude that no special corrections need to be made for axial resolution differences in either direct to cross slice comparisons or as a function of axial distance.

Fig. 9 shows the axial response profiles for the first 11 slices at the center and 9 cm from the center of the scan field. The direct slices are shown by solid lines, and the cross slices are dotted. The average slice-to-slice separation measured was 6.5

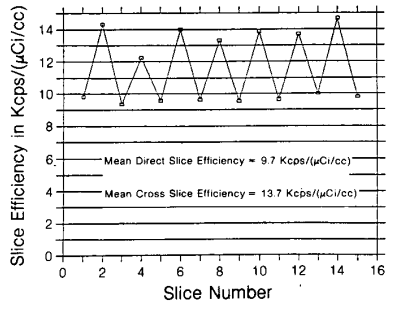

Fig. 3. Counting efficiency of the 15 slices of the PC-2048. The cross slices are approximately 40% more efficient than direct slices.

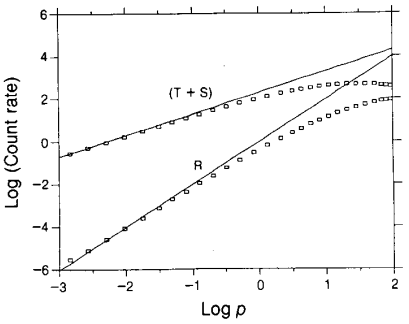

Fig. 4. Log-log plot of count rates from decay phantom, emphasizing the fitting of the low-activity points and subsequent extrapolation to high activity. Fitted curves (solid) have slopes of 1 and 2, respectively, for the $T + S$ and R components.

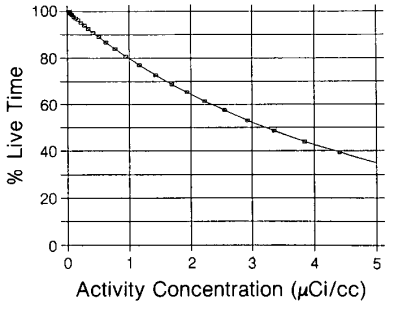

Fig. 5. Live-time versus activity concentration ρ. Note that at ρ = 0.8 μCi/cc, conditions approximating a bolus $H_2^{15}O$ study, the live-time is about 82%.

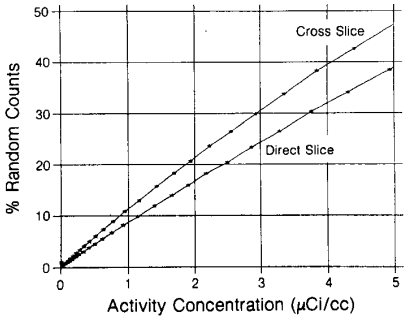

Fig. 6. Random fraction versus activity concentration ρ. Note that at ρ = 0.8 μCi/cc, conditions approximating a bolus $H_2^{15}O$ study, the random fraction is abut 8–9%.

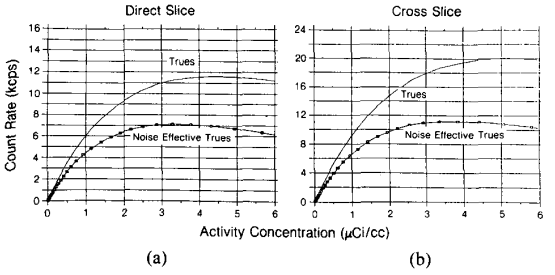

Fig. 7. Count-rate capability of the PC-2048 versus activity concentration, ρ, in a 19 cm diameter phantom. Data are shown with trues (T) only, i.e., with scattered (S) and random (R) events removed and as noise-effective trues T_{NE}, where $T_{NE} = T^2/(T + S + R)$.

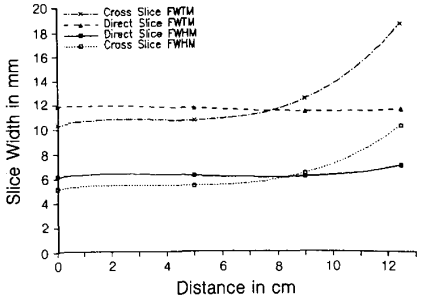

Fig. 8. Axial resolution of the PC-2048 versus radial position at FWHM and FWTM for both direct and cross slices. Note the relative uniformity over the inner 9 cm.

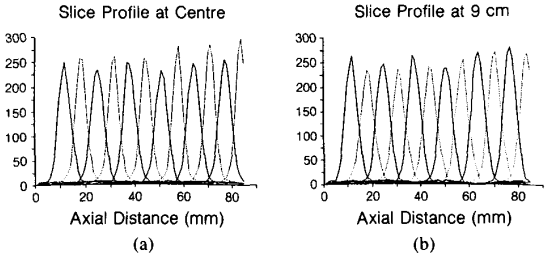

Fig. 9. Axial resolution profiles from the PC-2048. For each slice, reconstructed image counts at the center (a) and 9 cm out (b) are plotted as a function of source position.

mm. The slices are quite symmetric, and the intersections of all slice profiles occur at close to the mid-height point. This suggests that the axial volume could be adequately sampled, i.e., the Nyquist criterion satisfied, by taking two scans which are interleaved, since the sample width is slightly greater than the interslice separation. We are presently investigating this issue with the four-scan FDG control data and 3-D multiplanar reconstruction techniques.

D. Transverse Resolution

The optimum results for in-plane resolution (measured as FWHM and FWTM) were obtained using the Hann filter. The results for a 1 mm filter width for the wobbled, and 3.2 mm for stationary sampling, are plotted in Fig. 10 as a function of distance from the center of the field of view. The tangential component of the FWHM is relatively flat at 4.6–5.1 m for wobbled

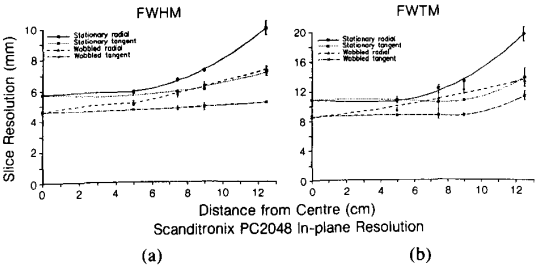

Fig. 10. Transverse resolution of the PC-2048 versus radial position for both stationary and wobbled acquisition modes. Curves are included for both FWHM (a) and FWTM (b). N.B. Filter used is the sharpest available for each mode (1 mm for wobble mode, 3.2 mm for stationary mode; see Fig. 12).

and 5.8–6.4 for stationary sampling over the range 0–9 cm from the center. From 9 to 12 cm, this component degrades more for stationary sampling. The radial component degrades progressively beyond 5 cm for both modes, and is 39% worse for wobbled mode, and 29% worse for stationary modes scans at 9 cm from the center. In general, the FWHM with stationary sampling remains 1 to 1.3 mm worse than with wobbled sampling throughout the normal field of view. There is a bigger progressive degradation of the FWTM for the stationary sampling scans. This is presumably due to under-sampling in angle towards the edge of the field of view.

The shape of the point spread function shows this more clearly in the isometric plots as a function of radial distance reproduced in Fig. 11. The functions from the stationary sampling case are quite misshapen compared to the wobbled sampling case.

The reconstructed resolution for both scanning modes of the Hann filter is plotted in Fig. 12 as a function of the filter width used for reconstruction. The difference in FWHM between stationary and wobbled modes, plotted in Fig. 12(a), increases from 0.6 mm to 1 as the reconstruction filter width increases from 3 to 10 mm. The difference in FWTM, shown in Fig. 12(b), is significantly greater, changing from 3 mm to 5 mm over the same interval. The measured FWHM from these fitted curves was used to determine the reconstructed resolution for the noise measurements in the next section. Note that these measurements were obtained in steel needles in air and, thus, do not include the effect of positron range. The actual image resolution will be slightly worse than these values, and will depend on the isotope used.

E. Image Noise as a Function of Scan Mode and Filter Width

The 17 cm diameter cylinder, which we use for cross calibration of the scanner and well counter, contained ^{68}Ge solution with a concentration of 50 nanoCi/cc. The average value in an ROI, including the central 80% of the cylinder, was measured to be the same for both scanning modes and all filter widths within 1%. The coefficient of variation (COV) in the ROI for wobbled and stationary scan modes for scans reconstructed from 100K and 400K counts was plotted against reconstructed FWHM and is shown in Fig. 13. For the wobbled studies, the COV halves between the first two filter widths. Comparing the first point on the 16 min study with the second point in the 4 min study, one sees that there is lower noise in a 4 min study reconstructed to 5.8 mm FWHM than in a 16 min study reconstructed to 5.1 mm.

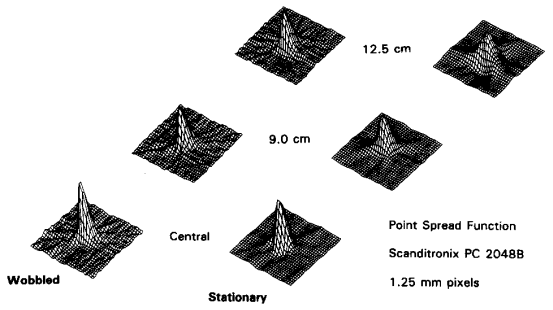

Fig. 11. Isometric plot of line spread function in wobbled and stationary modes for three different radial positions. Note the benefits of wobbling at all radial positions.

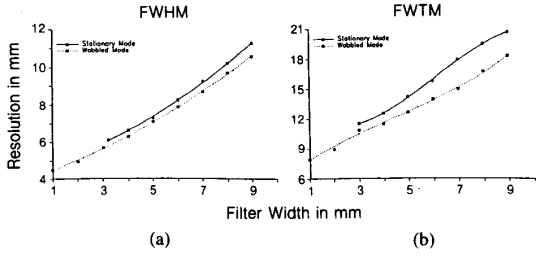

Fig. 12. Reconstructed resolution versus reconstruction filter width. Curves are shown for both FWHM (a) and FWTM (b) in both stationary and wobbled acquisition modes.

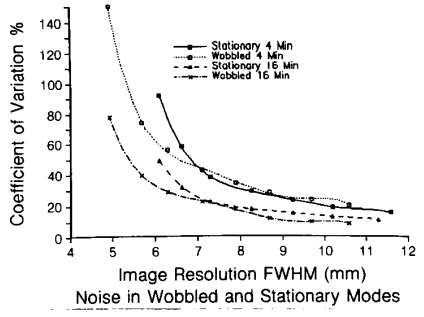

Fig. 13. Noise, expressed as a coefficient of variation within a circular ROI of 14 cm diameter placed over a flood phantom image, versus reconstructed resolution for two counting periods. The 4 min studies contains 100K counts and the 16 min study contains 400K counts. Note the benefits of wobbling are reduced as the reconstructed resolution degrades beyond about 7 mm.

As would be expected, at sharper resolution the wobbled mode scans have much less noise for a given counting time, and number of counts, than stationary mode scans. In the longer study, the wobbled scan always has the same or less for a given resolution than the stationary mode. Between 7 and 8 mm FWHM, the noise from both modes is almost equal, and beyond that the noise in the stationary mode is slightly lower in the shorter study.

F. Scatter Fraction

Fig. 14 shows the results obtained for the cool/cold spot phantom expressed as a percentage of the normalized background in each slice. The 25% cool spot is correctly recovered

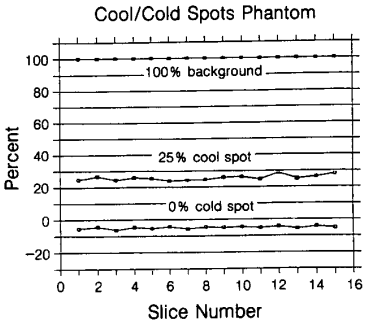

Fig. 14. Percentage recovery for 25% and 0% contrast inserts in a 19 cm flood phantom. The values are normalized to the average in 7 circular ROI's (3.5 cm diameter) distributed over the background region for each slice.

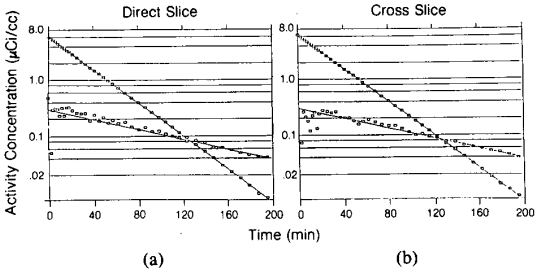

Fig. 15. Dual isotope experimental results for a direct and a cross slice from the PC-2048. Initially, ρ in the outer ^{11}C was 6 μCi/cc and the outer:inner contrast ratio was 20:1. Note the tendency to underestimate the cool spot in the cross slice for contrasts of 12:1 or higher.

in all slices but the cold spot was slightly overcorrected to a level of -4%.

G. Variable Contrast Recovery

Fig. 15(a), (b) shows the results of the dual isotope experiment expressed in semi-log form for both direct and cross slices. The direct slice data points show no obvious departure from the expected curves, but the cross slice data points show a tendency to underestimate the cool spot at contrasts greater than about 12:1.

H. Human Studies

Bolus $H_2^{15}O$: We have established the bolus $H_2^{15}O$ methodology for repeated CBF studies [15], [16] and are routinely conducting as many as 24 such studies in one day on the PC-2048 as part of existing projects in cognitive psychology and pain perception, obtaining results as exemplified by Fig. 16. Typical injected doses are between 30–40 mCi, yielding total image counts for the central planes of 250–350K during the 60 s following injection at a typical count-rate of 7–9 Kcps. When compared with Figs. 5–7, the bolus $H_2^{15}O$ methodology is well within acceptable limits for dead-time and random events.

FDG: We routinely perform FDG studies [17], [18] in the new system and, for patient studies, this is usually limited to a single 15-slice scan. In the eight control studies so far completed, kinetic FDG data was acquired followed by four interleaved 10-min scans to yield 60 FDG image planes at 1.7 mm axial spacing. A sample dataset, *collected under typical patient-imaging conditions*, is shown in Fig. 17.

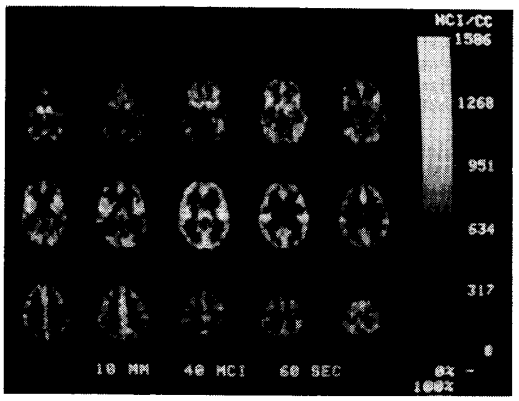

Fig. 16. 15-slice bolus $H_2^{15}O$ dataset collected on the PC-2048 without wobble and reconstructed with a 10 mm resolution filter. Data were collected over 60 s following injection of 35 mCi of $H_2^{15}O$. Central planes contain approximately 0.3M true counts.

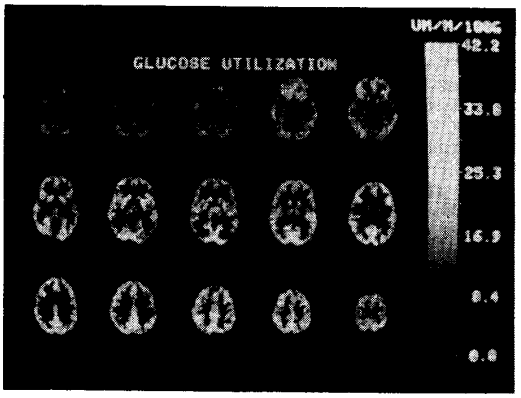

Fig. 17. 15-slice FDG dataset collected on the PC-2048 with wobble and reconstructed with a 6 mm FWHM resolution filter. Data were collected for 900 s, 45 min after a 5 mCi injection of FDG. Slices 7 and 8 contain 0.94M and true 1.27M counts.

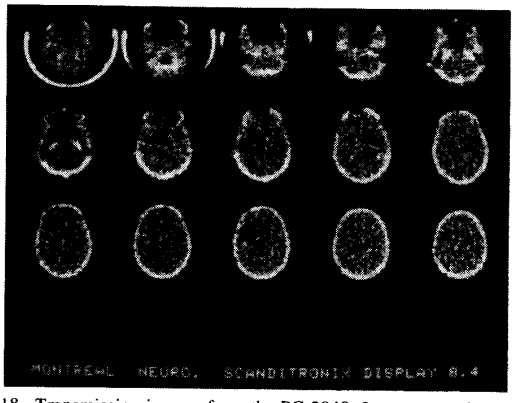

Fig. 18. Transmission images from the PC-2048. Images contain approximately 10M counts and were reconstructed at 4.5 mm resolution to emphasize the anatomical details particularly in the lower slices.

Transmission scans: The orbiting ^{68}Ge rod source is used for both detector normalization and transmission attenuation correction. We perform transmission studies prior to every emission study, scanning for 10 min prior to injection of the tracer. Typically, 10M true counts are collected per slice. For four-scan interleaved FDG studies, an equivalent four-scan transmission study is obtained. Fig. 18 shows an example of the transmission scans obtained by the PC-2048. This dataset was reconstructed to 4.5 mm resolution to emphasize the anatomical information available. This is most apparent in the lower slices where the petrous bones and other cranial vault structures are visible. For attenuation correction purposes only, the transmission image is usually smoothed to 10 mm resolution to reduce the propagation of noise into the emission image.

V. Discussion

The PC-2048 brain PET scanner recently installed at the MNI has a number of innovative features which require discussion. Most notably, the front end block crystal design in which 16 small BGO crystals are mounted on two dual PMT's in a 4 × 4 array. The crystal blocks used in this scanner are half the area of previous designs [19]. The principal purpose of the block design is to allow many small crystals to be coupled to four bulky PMT tubes and, hence, obtain higher spatial resolution than a 1:1 coupling would permit. The individual crystal in which a gamma ray interacts is determined by Anger-principle light division in both directions. The higher resolution is obtained at the potential cost of increased dead-time problems, since the entire block is paralyzed while the detecting crystal is being identified. The block dead-time is dependent upon the total flux across the block front surface, and, hence, for equivalent dead-time per event, larger blocks will be more susceptible to dead-time than smaller blocks. Total system dead-time can also be influenced by dead-time losses in the coincidence-processing electronics and the bandwidth of the computer interface. However, in the PC-2048, these other sources of dead-time are not significant compared with the block dead-time.

High Count-Rate Performance: The results summarized from Figs. 5–7 indicate that the PC-2048 count-rate saturates at a trues rate of 11.7 Kcps/s in a direct slice, with a concentration equivalent to approximately 5 μCi/cc in a 19 cm flood phantom. At present, bolus $H_2^{15}O$ CBF studies impose the highest count rate demands of the commonly applied neurological PET techniques. As shown by Fig. 16, a 35–50 mCi dose $H_2^{15}O$ produces excellent quality images in 40–60 s at a brain concentration equivalent to less than 1 μCi/cc. The results of Fig. 7 show that the noise effective count-rate peaks at an equivalent concentration of 3–4 μCi/cc. This suggests that doses as much as three times higher would further reduce noise in the images. The MNI ethics committee has established a dose limitation of 240 mCi for ^{15}O administered to human subjects in the form of $H_2^{15}O$. Given the quality of the images obtained with a 35–40 mCi dose (Fig. 16), we have chosen to partition this total into 6–7 separate smaller doses for rapid, serial CBF studies.

The quality of the dead-time and random corrections at high count-rate and any cross-contamination between random and scatter correction were tested by scanning a decay phantom with changing contrast (Fig. 15). Despite the extreme imaging conditions at the beginning of this dual isotope experiment (20:1 contrast ratio and a ρ of 6 μCi/cc at the start), the quantitative recovery of the PC-2048 was found to be acceptable well beyond the practical count-rate range. Evidence of over-correction for scatter was seen at contrasts of 12 to 1 or greater. This behavior was also apparent in the cold/cool spot experiment results shown in Fig. 14 where the off-center cold spot appeared at −4% instead of 0%. The central 25% cool spot was accu-

rately recovered and so this error may represent the limits of the scatter deconvolution correction, which has to approximate the behavior of the LSF as it approaches the edge of the scattering medium [11].

Resolution and Efficiency: As shown in Fig. 8, the axial resolution of the PC-2048 in the direct slice is quite uniform at the FWHM level while the cross slice resolution changes by 31% from center to 9 cm out. In Fig. 10, the radial transverse resolution of the scanner changes from 4.6 mm to 6.4 mm over a radial distance of 0–9 cm, a change of 39%. These latter changes, although a characteristic problem associated with smaller ring geometries, is an acceptable compromise to regain some counting efficiency. Since efficiency is inversely proportional to the square of the axial resolution, the goal of producing isotropic resolution demands a substantial price in lost efficiency. When considering the count-limited situations encountered in bolus $H_2^{15}O$ blood flow studies, Fig. 13 suggests that the benefits of wobbling the scanner are not significant for reconstruction filter widths of greater than 7 mm.

VI. Conclusion

In conclusion, the PC-2048 appears has satisfied the requirement of providing a practical reconstructed resolution in three dimensions of 5–6 mm while maintaining a count-rate performance necessary for bolus $H_2^{15}O$ studies of cerebral blood flow. Its near isotropic resolution and excellent resolution uniformity make it very suitable for three-dimensional imaging and quantification of brain chemistry and hemodynamics.

Acknowledgement

The authors wish to thank the Canadian Medical Research Council, the McConnell Foundation, and the Montreal Neurological Institute for their support in the purchase of the PC-2048. We appreciate the efforts of the staff and technicians of the MNI Positron Imaging Laboratories.

References

[1] A. C. Evans, C. J. Thompson, S. Marrett, R. Weltman, and S. Holte, "Performance characteristics of a high-resolution PET scanner for brain imaging in three dimensions," presented at Soc. Nucl. Med. Symp., St. Louis, MO, 1989.

[2] S. Holte *et al.*, "A preliminary evaluation of a positron camera system using weighted decoding of individual crystals," *IEEE Trans. Nucl. Sci.*, vol. 35, pp. 730–734, 1988.

[3] B. E. Cooke, A. C. Evans, E. O. Fanthome, R. Alarie, and A. M. Sendyk, "Performance figures and images from the Therascan 3128 positron emission tomograph," *IEEE Trans. Nucl. Sci.*, vol. 31, pp. 640–644.

[4] L. R. Carroll, P. Kertz, and G. Orcut, "The orbiting rod source: Improving performance in PET transmission correction scans," in *Emission Computed Tomography; Current Trends*. New York, Publishers: The Society of Nuclear Medicine, 1983.

[5] R. H. Huesman *et al.*, "Orbiting transmission source for positron tomography," *IEEE Trans. Nucl. Sci.*, vol. 35, pp. 735–739, 1988.

[6] N. T. Ranger, C. J. Thompson, and A. C. Evans, "The application of a masked orbiting transmission source for attenuation correction in PET," *J. Nucl. Med.*, vol. 30, pp. 1056–1068, 1989.

[7] C. J. Thompson, A. Dagher, D. N. Lunney, S. C. Strother, and A. C. Evans, "A technique to reject scattered radiation in PET transmission scans," in International workshop on physics and engineering of computerized multidimensional imaging and processing, *Pro. SPIE*, vol. 671, pp. 244–253, 1986.

[8] C. J. Thompson, A. Dagher, E. Meyer, and A. C. Evans, "Imaging performance of a dynamic positron emission tomograph: Positome IIIp," *IEEE Trans. Med. Imag.*, vol. 5, no. 4, pp. 183–198, 1986.

[9] C. J. Thompson, N. T. Ranger, and A. C. Evans, "Simultaneous transmission and emission scans in positron emission tomography," *IEEE Trans. Nucl. Sci.*, vol. 36, pp. 1011–1016, 1989.

[10] L. Eriksson, S. Holte, C. Bohm, M. Kesselberg, and B. Hovander, "Automated blood sampling system for positron emission tomography," *IEEE Trans. Nucl. Sci.*, vol. 35, pp. 703–707, 1988.

[11] M. Bergstrom, L. Eriksson, C. Bohm, G. Blomqvist, and J. Litton, "Correction for scattered radiation in a ring detector positron camera by integral transformation of the projections," *J. Comput. Assist. Tomogr.*, vol. 7, pp. 42–50, 1983.

[12] M. R. Palmer, M. Bergstrom, M. P. Beddoes, and B. D. Pate, "Effects of detector wobble motion on image noise in PET," *IEEE Trans. Med. Imag.*, vol. MI-4, pp. 58–62, 1985.

[13] M. E. Phelps, S.-C. Huang, E. J. Hoffman, D. Plummer, and R. E. Carson, "An analysis of signal amplification using small detectors in PET," *J. Comp. Asst. Tomogr.*, vol. 6, pp. 551–565, 1982.

[14] B. E. Cooke and A. C. Evans, "A phantom to assess quantitative recovery in positron tomograph," *J. Comput. Assist. Tomogr.*, pp. 876–880, 1983.

[15] P. Herscovitch, J. Markham, and M. E. Raichle, "Brain blood flow measured with intravenous $H_2^{15}O$ I. Theory and error analysis," *J. Nucl. Med.*, vol. 24, pp. 782–789, 1983.

[16] M. E. Raichle, W. R. W. Martin, P. Herscovitch, M. A. Mintun, and J. Markham, "Brain blood flow measured with intravenous $H_2^{15}O$ II. Implementation and validation," *J. Nucl. Med.*, vol. 24, pp. 790–798, 1983.

[17] M. Reivich, D. Kuhl, A. P. Wolf, J. Greenberg, M. Phelps, T. Ido, V. Casella, J. Fowler, E. Hoffman, A. Alavi, P. Som, and L. Sokoloff, "The 18-F-fluorodeoxyglucose method for the measurement of local cerebral glucose utilization in man," *Cir. Res.*, vol. 44, pp. 127–137, 1979.

[18] M. E. Phelps, S.-C. Huang, E. J. Hoffman, C. Selin, L. Sokoloff, and D. E. Kuhl, "Tomographic measurement of local cerebral glucose metabolic rate in humans with (F-18) 2-fluoro-2-deoxy-D-glucose: Validation of method," *Ann. Neurol.*, vol. 6, pp. 371–388, 1979.

[19] M. Dahlbom and E. J. Hoffman, "An evaluation of a two-dimensional array detector for high resolution PET," *IEEE Trans. Med. Imag.*, vol. MI-7, pp. 264–272, 1988.